



Cite this: *Nanoscale Adv.*, 2020, **2**, 4757

## Effects of gas-phase and wet-chemical surface treatments on substrates induced vertical, valley–hill & micro-granular growth morphologies of close space sublimated CdTe films†

Kulandai Velu Ramanathan,<sup>a</sup> Balakrishnan Shankar,<sup>b</sup> Shantikumar V. Nair<sup>a</sup> and Mariyappan Shanmugam  <sup>a</sup>

We implemented gas-phase (argon plasma) and wet-chemical ( $\text{HNO}_3$ ) surface treatments on close space sublimated (CSS) Cadmium Telluride (CdTe) thin films exhibiting morphologies of (i) vertically aligned walls on copper (Cu) and stainless steel (SS) substrates, (ii) valley–hills on aluminum (Al) substrates and (iii) micro-granules on nickel (Ni). As all the growth conditions (temperature, pressure, duration and source/substrate distance) were exactly the same in the CSS process to coat CdTe films, it is asserted that the various microstructures were raised only on Cu, Al, Ni and SS substrates. Plasma and  $\text{HNO}_3$  surface treatments on metal substrates did not affect the CdTe morphologies in terms of specific structures but it was observed that structural, optical and electrical charge transport characteristics were highly tunable by the two surface treatments. Thus, substrate driven morphological evaluation followed by surface treatments was enabled. The present study demonstrated various microstructures of CdTe films on metallic thin foil substrates to attempt the establishment of flexible opto-electronics based on CdTe.

Received 27th June 2020  
Accepted 15th August 2020

DOI: 10.1039/d0na00532k  
[rsc.li/nanoscale-advances](http://rsc.li/nanoscale-advances)

## Introduction

Light–matter interaction is the primary phenomenon which constitutes absorption, reflection, transmittance and scattering in semiconductors.<sup>1,2</sup> Mostly, nano-structural (zero, one, two and three dimensional such as quantum dots, nanofibers/rods/tubes, exfoliated individual atomically thin planes and bulk crystals) and optical (band gap and absorption coefficient) characteristics of semiconductors determine the efficiency of light–matter interactions.<sup>3–5</sup> Thus, it is evident that nano/micro-structures actively participate in light–matter interactions to determine essential factors which govern the primary opto-electronic characteristics of resulting semiconductor materials. While it has been identified that nano/micro-structures of thin films or the bulk of semiconductors can evidently alter light–matter interactions, the surface is also an essential factor at which the energy interaction begins.<sup>6–10</sup> The surface of thin films or bulk semiconductors becomes a dominant factor in the case of photon management as can be evidenced from various texture formations on the surface to minimize reflection

loss.<sup>11–15</sup> Textured semiconductor surfaces have been demonstrated to achieve minimum possible optical loss and increased optical path length which facilitated efficient exciton generation. Thus, surface morphology has been realized to be a dominant governing factor through which optical characteristics of semiconductors can effectively be engineered.<sup>16,17</sup>

The surface morphology of bulk and thin film semiconductors can be tailored by many different routes to achieve the desired optical features.<sup>18,19</sup> Plasma and wet-chemical environments have been envisaged to tailor structural, optical and electrical characteristics of semiconductors.<sup>20–23</sup> Plasma and wet-chemical treatments on thin film and bulk semiconductors can effectively enable doping, etching, polishing and surface modification which are all very interesting parameters for energy conversion technologies such as photovoltaics.<sup>24,25</sup> Additionally, surface treatments on semiconductors are essential routes through which all sort of disorders, in general defects, can be controlled.<sup>26,27</sup>

Cadmium Telluride (CdTe) has been studied intensively for various applications including photovoltaics,<sup>28–30</sup> nuclear radiation sensors,<sup>31</sup> photodetectors,<sup>32–34</sup> and medical imaging devices.<sup>35</sup> The structural, optical and electrical characteristics of CdTe are highly favourable for light–matter interaction and thus it is one of the highly appreciated functional materials in energy conversion science and technology.<sup>36–38</sup> Specifically, the optical bandgap of CdTe (1.5 eV)<sup>39</sup> is an exceptional parameter which deserves special attention for the requirements of the

<sup>a</sup>Amrita Centre for Nanosciences and Molecular Medicine, Amrita Vishwa Vidyapeetham, Kochi, Kerala – 682041, India. E-mail: [mshanmugham@aims.amrita.edu](mailto:mshanmugham@aims.amrita.edu)

<sup>b</sup>Department of Mechanical Engineering, Amrita Vishwa Vidyapeetham, Amritapuri, Kerala – 690525, India

† Electronic supplementary information (ESI) available. See DOI: [10.1039/d0na00532k](https://doi.org/10.1039/d0na00532k)



Shockley-Queisser detailed balance limit.<sup>40</sup> CdTe has promising applications in thin film solar cells competing with silicon, gallium arsenide and copper indium diselenide due to its optimum direct bandgap to cover the visible solar spectrum with an exceptionally high absorption coefficient.<sup>41,42</sup> Thus, it has been predicted and demonstrated that a nearly 2  $\mu\text{m}$  CdTe film is sufficient to absorb incident photons completely.<sup>43</sup> Thin film CdTe has been processed by several methods including close space sublimation (CSS),<sup>44</sup> RF-sputtering,<sup>45</sup> electron beam evaporation<sup>46</sup> and wet-chemical methods.<sup>47</sup>

While CdTe has successfully shown its record benchmark efficiency in various applications including photovoltaics, surface/interface defects are considered to be dominant factors which eventually limit the performance in terms of light-matter interaction, charge transport kinetics, carrier lifetime and overall efficiency of the resulting applications.<sup>48–50</sup> Thus, it is an essential requirement to achieve efficient surface passivation schemes which can effectively alter and control the role of surface/interface defects on the functionality of CdTe films. In general, wet-chemical surface treatment has widely been established to enhance the quality of CdTe in terms of crystallinity, conductivity, minimized grain boundaries, and maximized grains which are all essential factors to determine the overall performance of the resulting applications.<sup>51,52</sup> Surface treatment methodologies are direct routes to suppressing the active defects which efficiently participate in the charge transport in CdTe and play detrimental role as evidenced from previous studies.<sup>53,54</sup> Specifically, density and activity (trapping, de-trapping and scattering) of surface and interface defects in CdTe, when it reaches the nanoscale regime, become important factors which govern light-matter interactions and follow various physical processes. However, it is favourable to implement nanostructures of CdTe in all sorts of functional applications as they show promising structural advantages in the resulting products. Thus, surface treatment methods are highly justified in the case of nanostructured CdTe to engineer the surface/interface defects.

The present work adequately addresses the possibility of obtaining three different microstructures on flexible metallic foil substrates followed by two surface treatments to engineer the morphology and charge transport kinetics. In short, we report (i) vertically aligned walls, (ii) valley-hills and (iii) micro-granules on Cu/SS, Al and Ni substrates, respectively. Further, the substrate induced CdTe microstructures were subjected to gas-phase (Ar plasma) and wet-chemical ( $\text{HNO}_3$ ) surface treatments to examine their roles in structural, optical and charge transport characteristics.

## Experimental section

We performed CdTe film growth on Cu, Al, Ni and SS metal foils. All the four categories of metal foil were divided into three sets. The first set of all four metal foils was subjected to ultrasonic cleaning with deionized water, isopropyl alcohol and acetone as a standard cleaning procedure. The second set of four metal foils was subjected to a treatment with 1 : 2 ratio solutions of  $\text{HNO}_3$  and DI water prepared in a bath. The four

metal foils were immersed in the bath for 1 minute and dried at 70 °C and then rinsed with DI water. The third set of metal foils was exposed to RF-plasma generated by 50 sccm of argon gas with 150 W RF-power. The plasma exposure was performed for 30 minutes. All three sets of samples were loaded into a high vacuum CSS chamber for CdTe film deposition. We used 99.99% pure CdTe source powder, obtained from Alfa Aesar, filled evenly in a graphite crucible. The CdTe film was coated at a base pressure of  $1 \times 10^{-6}$  mbar with a growth temperature maintained at 555 °C ( $T_G$ ) and substrate temperature of 330 °C ( $T_S$ ). The duration of CdTe film growth was maintained (20 minutes) for all substrates to obtain uniformity in terms of thickness. Table 1 lists material and CSS process related details in brief. Fig. 1 shows digital photographic images of (a) rolled Al foil before and after coating the CdTe film. In order to test the uniformity and continuity of the CdTe film on a larger area, we coated the CdTe film on 8  $\text{cm}^2$  Al foil as shown in Fig. 1(b). Similar attempts were made on Cu foil as shown in Fig. 1(c) and (d) showing CdTe films coated on rolled and large area Cu foil, respectively. The top and bottom images in (e) show Ni foil before and after CdTe coating, respectively. The top and bottom images in (f) show SS foil before and after CdTe coating, respectively.

The CSS processed CdTe films on four substrates with two surface treatments were subjected to field emission scanning electron microscopy (FESEM) studies to examine the surface morphology using a JSM 7610S Plus JEOL-JSM-6490-LA scanning electron microscope. X-ray diffraction (XRD) measurements were performed on all CdTe samples using a PANalytical X'Pert PRO X-ray diffractometer. Further, the values of the average crystallite sizes of CdTe samples were calculated using the Debye-Scherrer equation. UV-visible optical absorption measurements were performed on CdTe samples using a PerkinElmer Lambda-750 spectrophotometer. In order to evaluate charge transport kinetics in CdTe to assess the effect of morphology and surface treatments, we fabricated two terminal device configurations using carbon as ohmic contacts with a spacing of 0.5 mm. The current-voltage ( $I-V$ ) characteristics of CdTe films were measured under dark and illuminated conditions in a Probe Station equipped with a Keithley 2420 source meter in an applied bias region of –5 V to 5 V.

## Results and discussion

The three SEM images shown in column 1 of Fig. 2 show low-magnification surface morphologies of the pristine,  $\text{HNO}_3$  and plasma treated Cu foil used for CdTe coating in the CSS process.

**Table 1** Specifications of metallic foil substrates used in the CSS process to coat CdTe films

Substrates	Purity/grade	Thickness	Manufacturer	CdTe $T_G/T_S$ (°C)
Cu	99.99%	024 $\mu\text{m}$	MTI Corp.	555/330
Al	99.30%	015 $\mu\text{m}$	MTI Corp.	555/330
Ni	99.00%	500 $\mu\text{m}$	—	555/330
SS	SS 316	100 $\mu\text{m}$	MTI Corp.	555/330



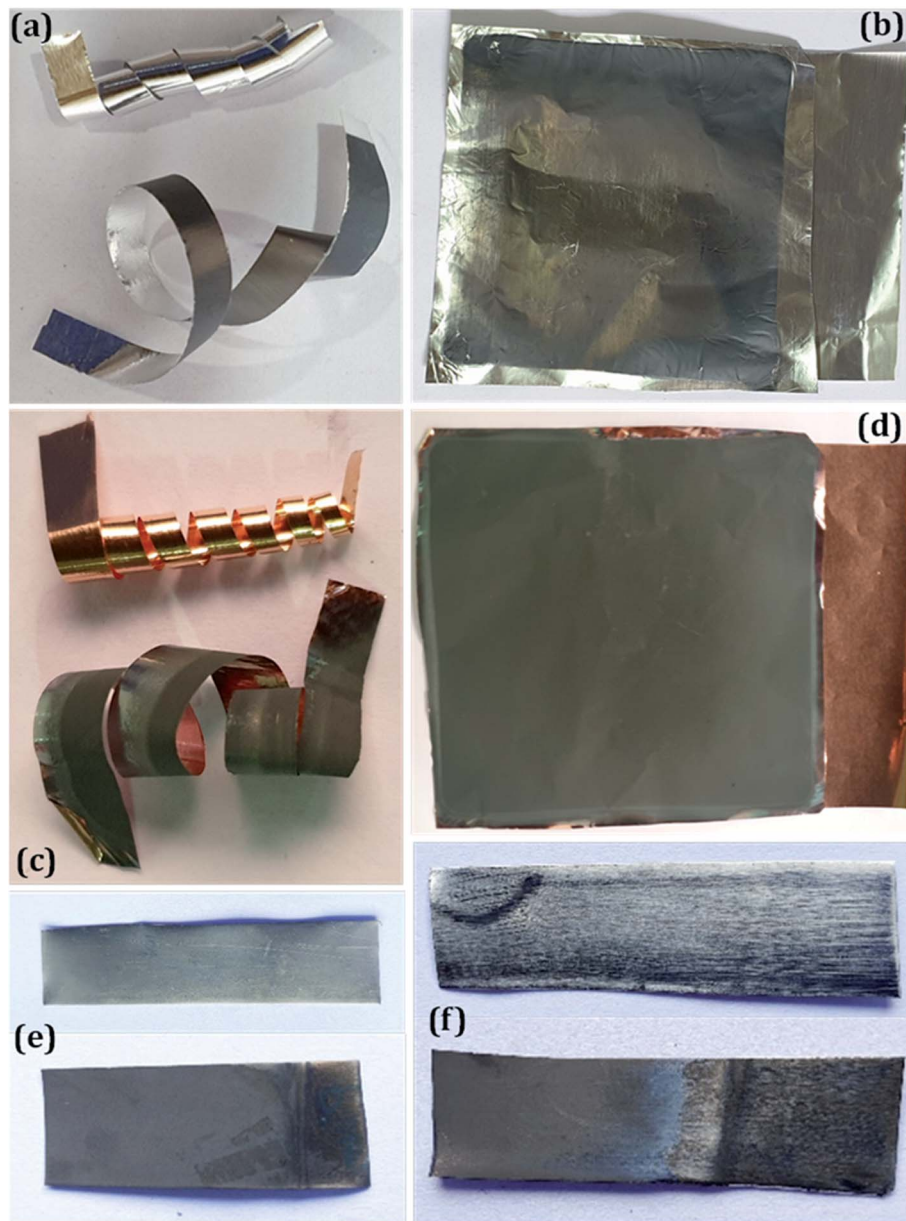


Fig. 1 Digital images of CdTe films coated on (a) rolled and (b) large area Al foil. (c) and (d) CdTe films coated on rolled and large area Cu foil, respectively. Top and bottom images in (e) show Ni foil before and after CdTe coating, respectively. Top and bottom images in (f) show SS foil before and after CdTe coating, respectively.

The three SEM images shown in column 2 are the surface morphologies of CdTe films coated on pristine,  $\text{HNO}_3$  and plasma treated Cu foil using the CSS process. All the three CdTe surface morphologies were acquired at a magnification of  $1000\times$ . Column 3 in Fig. 2 shows higher magnification ( $20\,000\times$ ) SEM images of column 2 to show the microstructures of CdTe films clearly. The very first observation was that CSS yielded crack-free and continuous CdTe growth on all three Cu substrates. CdTe growth on pristine Cu foil was found to be vertically oriented micron-size platelets distributed randomly as can be evidenced from column 2 in Fig. 2. At a magnification of  $20\,000\times$ , it can be evidenced that the CSS process yielded flat-terminated vertically oriented platelets. This means that the

platelets were well-faceted and did not show any sharply terminated edges as can be realized from the SEM images listed in column 3. In Fig. 2, row 2 shows the microstructures of the CdTe film grown on Cu foil which was treated with  $\text{HNO}_3$  as detailed in the Experimental section. The first SEM image in row 2 represent the surface morphology of the  $\text{HNO}_3$  treated Cu foil and the other two show the surface morphologies of CdTe films at  $5000\times$  and  $20\,000\times$  on  $\text{HNO}_3$  treated Cu foil. As we did not make any other changes in the CSS process, such as pressure and temperature, except the  $\text{HNO}_3$  treatment on Cu foil, it is direct evidence that the morphology change occurred due to the surface treatment. Compared with the SEM images in row 1, the microstructures shown in row 2 demonstrated less-densely



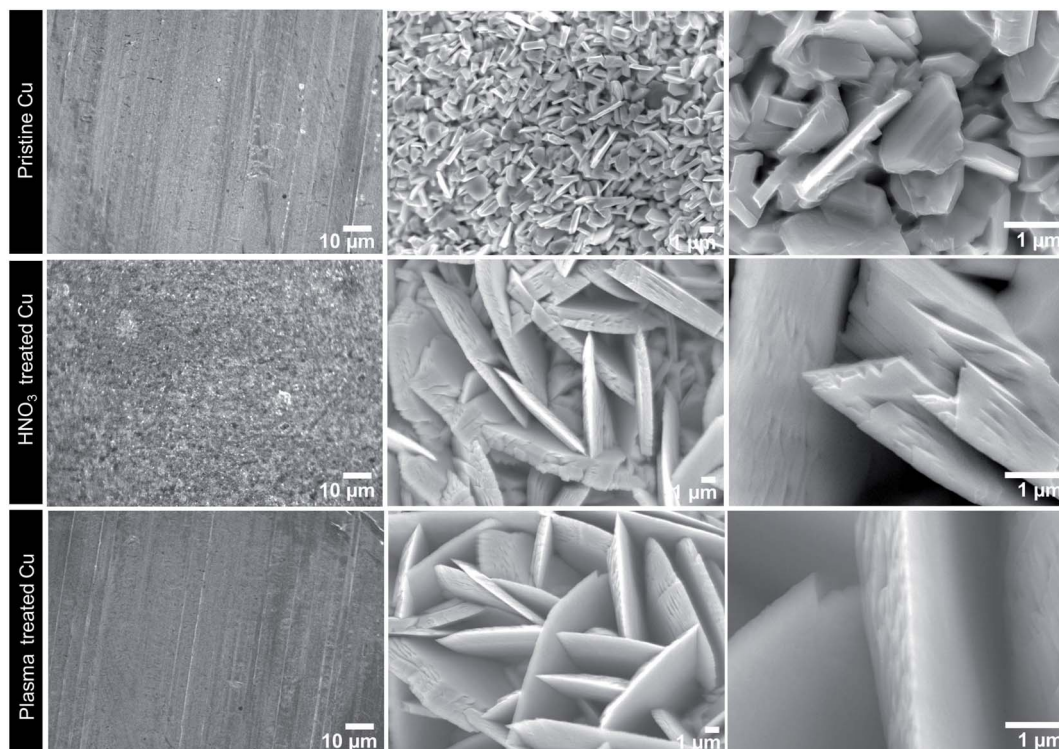


Fig. 2 Microstructural evolution of CdTe films on pristine,  $\text{HNO}_3$  and plasma treated Cu foil. Column 1 represents the morphology of Cu foil before CdTe coating.

distributed CdTe. Further, it is important to observe that the edges of the CdTe platelets were sharpened very well and the entire microstructure shown in row 1 was evidently transformed into vertically aligned wall-like shapes. This change is attributed to  $\text{HNO}_3$  treatment on Cu foil which essentially changed the surface energy that could lead to the growth of CdTe in a very different manner in comparison with CdTe growth that occurred on pristine Cu foil.

Similar to the effect of  $\text{HNO}_3$  treatment on Cu foil, the present study also evaluated CdTe growth on Cu foil treated with Ar plasma as explained in the Experimental section. As shown in row 3, the CdTe microstructures observed at 5000 $\times$  and 20 000 $\times$  magnifications show significant changes in morphology in comparison with CdTe grown on pristine Cu foil but very similar to the CdTe on  $\text{HNO}_3$  treated Cu foil. Thus, it can be concluded that surface treatment in terms of both wet-chemical and gas phase effectively alters the surface-chemical nature of Cu foil as a substrate. The change in the surface-chemical nature established by both  $\text{HNO}_3$  and plasma treatment is attributed to the change in morphology from platelets to vertically oriented wall-like structures with sharp edges.

The microstructures of CdTe films grown on Al foil are shown in Fig. 3. The three SEM images in column 1 of Fig. 3 show the low-magnification surface morphologies of the pristine,  $\text{HNO}_3$  and plasma treated Al foil. The three SEM images in column 2 show the surface morphologies of CdTe films coated on pristine,  $\text{HNO}_3$  and plasma treated Al foil. All the three CdTe surface morphologies, shown in column 2, were acquired at

a magnification of 5000 $\times$ . Column 3 in Fig. 3 shows the higher magnification (20 000 $\times$ ) SEM images of column 2. The CdTe growth on pristine Al foil resulted in valley-hill structures of different sizes. This feature was observed only on pristine Al foil which was further treated with  $\text{HNO}_3$  and Ar plasma. The corresponding microstructures are shown in rows 2 and 3 in Fig. 3. It is evident from the SEM images shown in rows 2 and 3 that the valley-hill type of microstructures were collated into uniformly distributed CdTe clusters. It is clear that  $\text{HNO}_3$  and plasma act on the CdTe valley-hills which were eventually engineered as micro-clusters. It was also observed that the wet-chemical and gas-phase surface treatments can re-orient and redistribute the growth morphologies to a great extent as evidenced from the morphologies shown in the three rows corresponding to pristine,  $\text{HNO}_3$  and plasma treated Al foil. It is further envisaged that  $\text{HNO}_3$  and plasma treatments on Al foil altered the surface energy distribution which limits the valley-hill type of growth and facilitated the formation of micro clusters. In other words, it is possible to attribute the formation of clusters on surface treated Al foil to the limitation of increasing selective area preferred growth as it leads to the formation of valleys and hills consecutively. As the growth of hills was suppressed and valleys were filled due to the  $\text{HNO}_3$  and plasma treatments on Al foil, it is possible to obtain uniform distribution of micro-clustered CdTe as shown in the microstructures in rows 2 and 3. In comparison with  $\text{HNO}_3$  and Ar plasma treatment, it is rather difficult to identify the changes in microstructures as they were very similar. However, it was observed



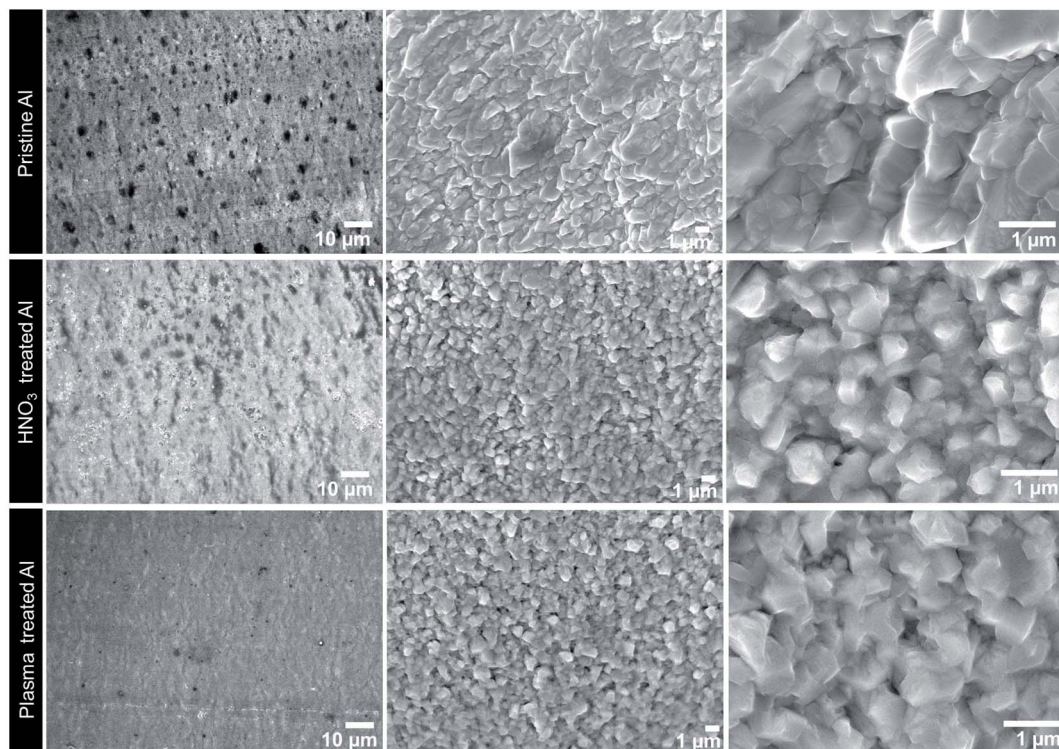


Fig. 3 Microstructural evolution of CdTe films on pristine,  $\text{HNO}_3$  and plasma treated Al foil. Column 1 represents the morphology of Al foil before CdTe coating.

that plasma treatment damaged the micro-clusters in terms of size and distribution as can be visualized in the  $20\,000\times$  magnified image shown in column 3. This could be due to the high energy interaction of Ar ions on the surface of Al foil which yielded different surface environment for the growth of CdTe in the CSS process. Overall, the microstructures on Al foil were significantly different from those on Cu foil as can be compared with Fig. 2.

Column 1 of Fig. 4 shows the low-magnification surface morphologies of the pristine,  $\text{HNO}_3$  and plasma treated Ni foil used for CdTe coating. The three SEM images in column 2 show the surface morphologies of CdTe films coated on pristine,  $\text{HNO}_3$  and plasma treated Ni foil. All the three CdTe surface morphologies were acquired at a magnification of  $5000\times$ . Column 3 in Fig. 4 shows the higher magnification ( $20\,000\times$ ) SEM images of column 2 to show the microstructural evolution of the CdTe films clearly.

It was observed that loosely packed micro-granular CdTe particles were randomly distributed on Ni foil. The first, second and third rows in Fig. 4 represent CdTe on pristine,  $\text{HNO}_3$  and plasma treated Ni foil, respectively. Compared with CdTe on Cu and Al foil, it is evident that Ni yielded entirely different microstructures which can be considered loosely packed micro-granular particles. It is also possible to define the CdTe film as porous as we can see the voids among the distributed CdTe particles. Row 2 in Fig. 4 shows the variation of CdTe micro-granules due to the  $\text{HNO}_3$  treatment. It is visualized that the granules were well isolated due to the  $\text{HNO}_3$  treatment in

comparison with CdTe granules on pristine Ni foil. The wet-chemical treatment diffused into the microstructural voids of the film and edged the granules which resulted in granules with well-defined facets. Ar plasma treatment was observed to yield a granular structure with little increase in size as can be roughly estimated from the higher magnification SEM image shown in row 3.

The three SEM images in column 1 of Fig. 5 show the low-magnification surface morphologies of the pristine,  $\text{HNO}_3$  and plasma treated SS foil. The three SEM images in column 2 show the surface morphologies of CdTe films coated on pristine,  $\text{HNO}_3$  and plasma treated SS foil. All the three CdTe surface morphologies were acquired at a magnification of  $5000\times$ . Column 3 in Fig. 5 shows higher magnification ( $20\,000\times$ ) SEM images of column 2 to show the microstructures of CdTe films on SS foil clearly.

Row 1 in Fig. 5 shows vertically oriented CdTe microstructures on pristine SS foil. In the case of SS, unlike Ni, the vertically grown CdTe was observed to be densely packed as can be visualised at three different magnifications. It is important to observe that  $\text{HNO}_3$  treatment on SS foil completely ruined the formation of microstructures as shown in the SEM images in row 2. In contrast, Ar plasma treatment on SS foil established the vertically aligned CdTe microstructures as presented in row 3.

The XRD pattern of CdTe on pristine Cu foil shown in Fig. 6(a) shows the polycrystalline nature of CdTe grown along the crystal orientation of Cu foil which can be seen in the XRD



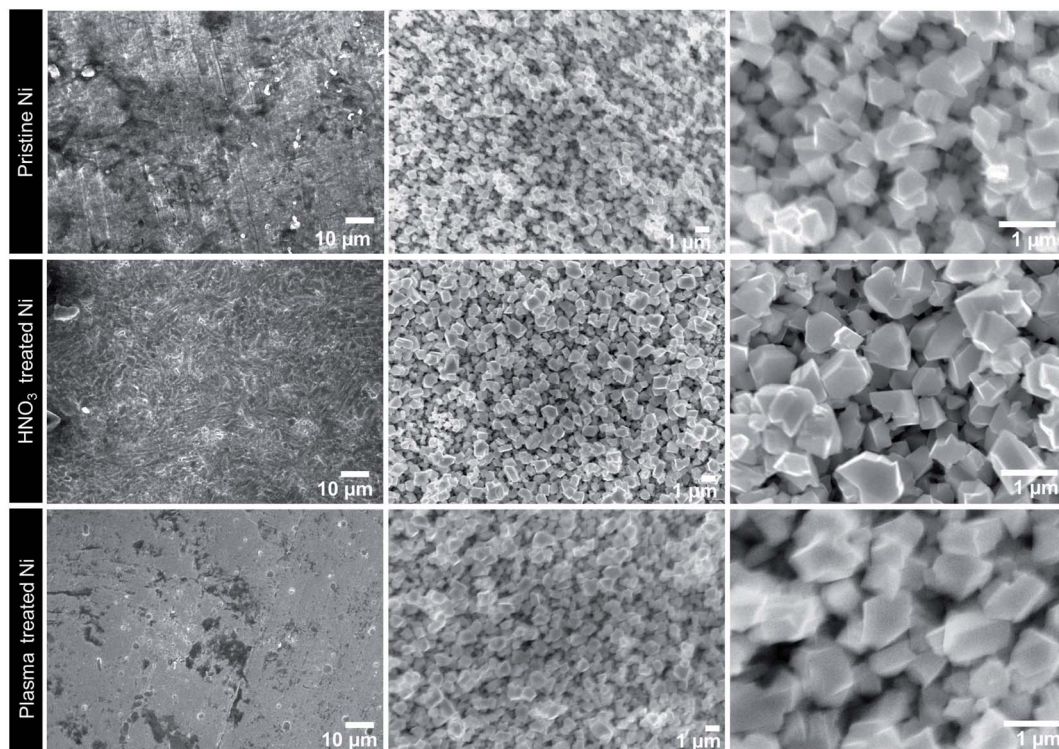


Fig. 4 Microstructural evolution of CdTe films on pristine,  $\text{HNO}_3$  and plasma treated Cu foil. Column 1 represents the morphology of Ni foil before CdTe coating.

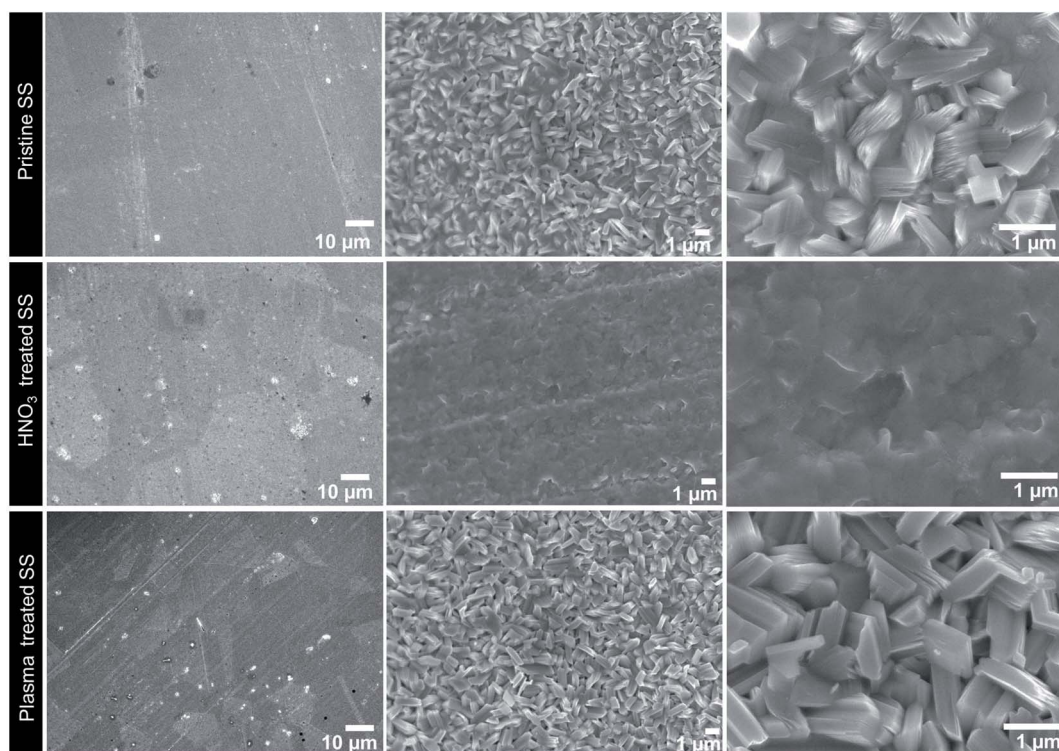


Fig. 5 Microstructural evolution of CdTe films on pristine,  $\text{HNO}_3$  and plasma treated SS foil. Column 1 shows the morphology of SS foil before CdTe coating.

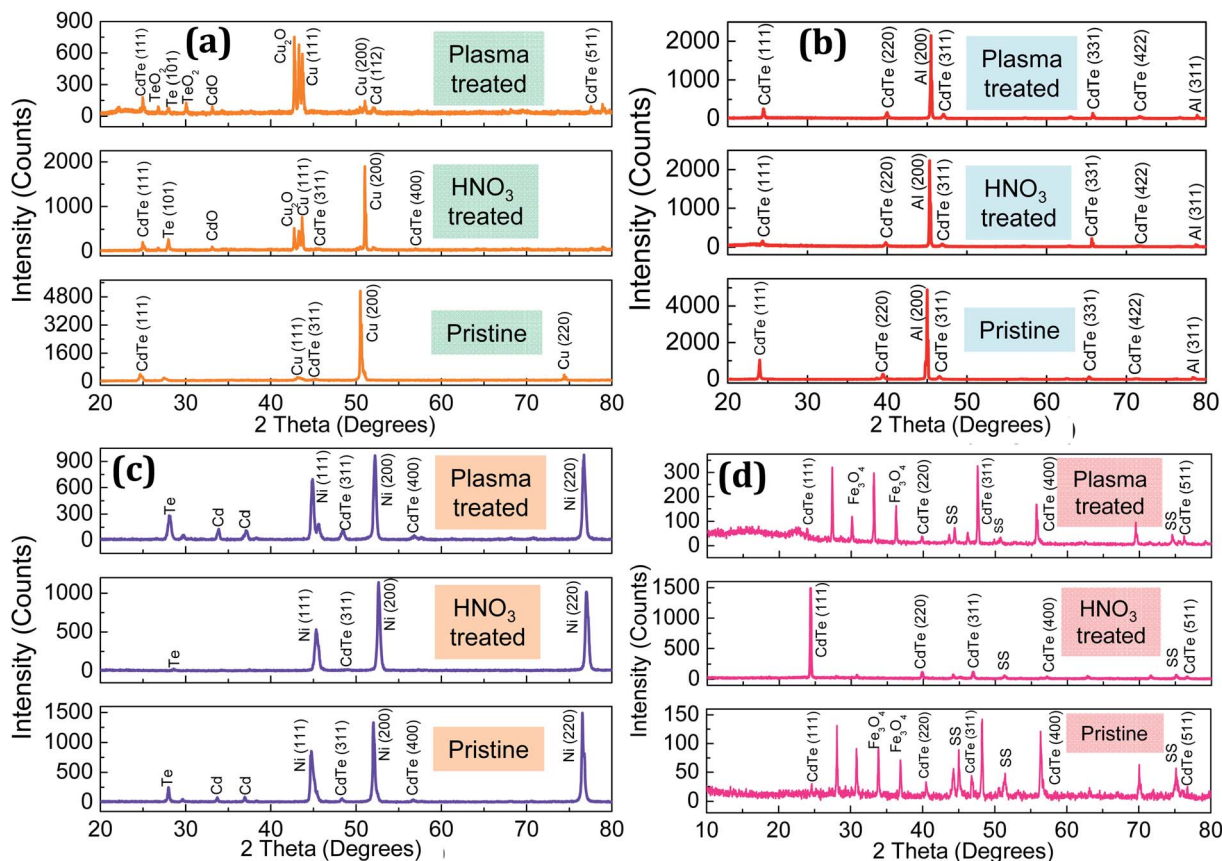


Fig. 6 XRD patterns obtained from the CdTe films grown on (a) Cu, (b) Al, (c) Ni and (d) SS foil showing the variation due to  $\text{HNO}_3$  and plasma treatments.

pattern with the high intensity peak of CdTe (111) at 24.685°, as reported elsewhere,<sup>55,56</sup> along with Cu's high intensity peak (111) at 43.165°, with the other significant peak of CdTe (311) at 45.205° along with Cu (200) and Cu (220) at 50.515° and 74.425°, respectively. These values are in good agreement with previous studies.<sup>31,33</sup> However, when treated with HNO<sub>3</sub> the introduction of oxides in Cu gives rise to Cu<sub>2</sub>O and CdO peaks at 42.735° and 33.155°, respectively, with CdTe peaks at 24.975° (111), 45.715° (311), and 56.945° (400) along with the elemental Te (101) peak at 27.995° and substrate Cu peaks at 43.675° (111) and 51.025° (200). The plasma treated Cu substrate also contained oxides with the presence of TeO<sub>2</sub> with peaks at 26.795° and 30.065°, the CdO peak at 33.135° and the Cu<sub>2</sub>O peak at 42.755°, while CdTe grown on top of this substrate exhibited CdTe peaks at 24.975° (111) and 77.575° (511) and Cu peaks at 43.305° (111) and 51.035° (200). The plasma treated Cu substrate with CdTe also shows elemental Te and Cd with 28.005° (101) and 52.005°, respectively. The presence of elemental Te and oxide compounds in HNO<sub>3</sub> and plasma surface treated substrates can be related to the growth of wall-like structures with sharp edges as discussed previously. Fig. 6(b) shows the XRD pattern obtained from CdTe on the Al substrate. It was observed that the (200) and (311) peaks of Al in pristine foil at 45.025° and 78.325° were shifted to 45.325° and 78.725° with HNO<sub>3</sub> treatment and further shifted to 45.495° and 78.905° with plasma treatment.

respectively. The CdTe grown on top of pristine Al foil has (111), (220), (311), (331) and (422) peaks at  $23.995^\circ$ ,  $39.445^\circ$ ,  $46.555^\circ$ ,  $65.335^\circ$  and  $71.185^\circ$ , respectively, with a shift for all the peaks to  $24.375^\circ$ ,  $39.815^\circ$ ,  $46.915^\circ$ ,  $65.675^\circ$  and  $71.565^\circ$  for  $\text{HNO}_3$  treated substrates and a further shift when treated with plasma to  $24.455^\circ$ ,  $39.995^\circ$ ,  $47.105^\circ$ ,  $65.785^\circ$  and  $71.665^\circ$ , respectively, as reported elsewhere.<sup>31,33</sup> The shift in the  $2\theta$  values of CdTe shows the change in the crystal structure with the strain placed on the lattice due to the change in surface orientation of Al foil due to the surface treatments. The shift of Al peaks with respect to the treatments evidently provides us clarity on the replacement of the valley-hill structure with micro-clusters.

Fig. 6(c) shows the XRD pattern of CdTe on Ni substrates. Unlike other types of foil, the pristine nickel substrate induced the presence of elemental Cd at  $33.715^\circ$  and  $36.925^\circ$  along with elemental Te at  $27.985^\circ$  as shown in the XRD pattern. The modifications in Ni foil give rise to peaks at  $44.755^\circ$  (111),  $52.045^\circ$  (200) and  $76.555^\circ$  (220) whereas the peaks shift to  $45.325^\circ$ ,  $52.645^\circ$  and  $77.035^\circ$  when treated with  $\text{HNO}_3$  and to  $44.905^\circ$ ,  $52.225^\circ$  and  $76.735^\circ$  when treated with plasma.<sup>31,33</sup>

The appearance of the elemental peak of Te at  $28.585^\circ$  for the  $\text{HNO}_3$  treated film and  $28.075^\circ$  for plasma treatment in addition to elemental Cd peaks at  $33.895^\circ$  and  $37.075^\circ$  for plasma treated foil with the absence of Cd in  $\text{HNO}_3$  treated films evidently showed the disruption in the nucleation process. However, the

common CdTe high intensity peak at (111) was missing due to the oriented growth of the films with (311) and (400) at 48.355° and 56.695° for pristine Ni foil, while the (311) peak was at 49.015° for the HNO<sub>3</sub> treated film with the (311) peak at 48.505° and (400) peak at 56.815° for plasma treated foil as shown in Fig. 6(c).<sup>31,33</sup> Fig. 6(d) shows the XRD patterns obtained from SS substrates. The presence of Fe<sub>3</sub>O<sub>4</sub> in the pristine SS foil at 33.865° and 36.895° was also observed in plasma treated foil at 33.145° and 36.235° but Fe<sub>3</sub>O<sub>4</sub> was removed when treated with HNO<sub>3</sub> changing the morphology of CdTe as shown in the SEM micrographs. The other SS peaks were found at 45.025°, 51.445° and 75.175° in pristine foil with peaks at 46.915° and 75.115° for HNO<sub>3</sub> treated foil, and in plasma treated foil the peaks were at 44.335°, 50.725° and 74.545°. The presence of CdTe was confirmed by the CdTe (111) peak at 24.625° along with the (220) peak at 40.465°, (311) peak at 46.795°, (400) peak at 56.365° and (511) peak at 76.705°. The peaks of CdTe on HNO<sub>3</sub> treated SS foil can be seen at 24.355° (111), 39.835° (220), 57.175° (400) and 76.645° (511) while the CdTe peaks on plasma treated foil are at 23.845° (111), 39.805° (220), 47.545° (311), 55.705° (400) and 76.195° (511) in the XRD data. The average crystallite sizes of all CdTe samples coated on pristine, HNO<sub>3</sub> and plasma treated Cu, Al, Ni and SS substrates are listed in Table 2.

As CSS is a process which involves temperature triggered nucleation of CdTe on the surface of the substrates, nucleation and growth of polycrystalline films includes the role of nucleus density, nucleus size and the Volmer–Weber mechanism. The density of the nuclei is dependent on the substrate temperature, where a low temperature process provides the nuclei with high density and *vice versa*. As the nucleus density also relies upon the surface energy of the substrate which determines the atomic mobility at the surface of the substrate, here we have treated pristine metal substrates with diluted HNO<sub>3</sub> acid and high energy plasma modifying the surface energy and orientation of the metal substrates. This change in substrate properties leads to variation in atomic mobility and nucleus density of the CdTe deposited. The atomic mobility of CdTe molecules at the surface of substrates adds together to form a large nucleus with high interfacial energy. Therefore atomic mobility in the surface varies from substrate to substrate as surface energy is varied. The interface between CdTe and the metal substrate gives rise to interfacial energy which determines the initial orientation of the polycrystalline film grown on top of the substrate. However, nuclei with low interfacial energy attach to the nuclei with high

interfacial energy leading to the preferred orientation of the film.

The nuclei attach to each other to form grains and grain boundaries with wide-ranging sizes subject to the thickness of the film. These grains form islands in the substrate which gather based on diffusion of molecules. The diffusion rate of the molecules is influenced by the surface energy of the substrate which is associated with the free energy of the molecules. A driving force based on the configuration and properties of the substrates initiates reduction in free energy allowing molecules to diffuse into grain boundaries in one direction and controls the free movement of molecules between grains. It facilitated the formation of larger grains in CdTe with less number of grain boundaries.

In this work, we have deposited CdTe on pristine, HNO<sub>3</sub> and plasma treated metal foil pieces of Cu, Al, Ni and SS. On Cu foil the growth of CdTe resembles platelet structures with growth in the grain size due to HNO<sub>3</sub> and plasma treated foil whereas the grain size of CdTe on pristine Cu foil is smaller. As inferred from the above mechanism we can understand that the interfacial energy between Cu and CdTe was improved by different treatments and the atomic mobility of molecules was also improved. From the XRD patterns it is clear that oxides of Cu, Cd and Te are present in both acid and plasma treated substrates identifying the change in the surface of Cu foil. In Al foil the grain growth was affected by the modified surface resulting in an increase in the free energy of the molecules with a reduced diffusion rate of the molecules. Hence the grain growth was enormous in pristine Al foil compared to that in the treated foil pieces. Unlike Cu foil, Al did not retain atmospheric oxygen on its surface; however, a slight shift in the high intensity peak of Al shows us the tensile stress created at the surface.

In Ni foil, stability of the grain size was observed indicating that the change in surface energy due to HNO<sub>3</sub> and plasma treatment on the surface doesn't affect the microstructures of CdTe. But the XRD pattern shows us the difference in the composition of Cd and Te in the polycrystalline CdTe film grown on different Ni substrates. In SS foil, CdTe grains resembled a vertically aligned wall-like structure predominant in pristine and plasma treated SS foil, whereas in HNO<sub>3</sub> treated SS foil, it is not surprising to see destruction in microstructures, since the modification in surface energy is capable of allowing this growth. The presence of Fe<sub>3</sub>O<sub>4</sub> peaks in pristine and plasma treated SS foil matches the micrographs while HNO<sub>3</sub> treated SS foil lacks the Fe<sub>3</sub>O<sub>4</sub> peaks.

Fig. 7 shows the UV-visible optical absorption measurements performed for CdTe films grown on (a) Cu, (b) Al, (c) Ni and (d) SS foil in the wavelength range of 350–850 nm. The measurements clearly show the variation in absorption of CdTe films due to HNO<sub>3</sub> and plasma treatment with respect to the CdTe grown on pristine substrates.

In the case of CdTe grown on the Cu substrate, HNO<sub>3</sub> treatment increased the absorbance and plasma treatment suppressed the magnitude as the morphology change influenced the interaction with photons. Moreover, the characteristics were also not saturated well in the longer wavelength side

**Table 2** Values of average crystallite sizes estimated using the Debye–Scherrer equation

Substrates	Average crystallite sizes (nm)		
	Pristine	HNO <sub>3</sub> treated	Plasma treated
Cu	190	535	536
Al	496	313	416
Ni	238	124	196
SS	502	605	254



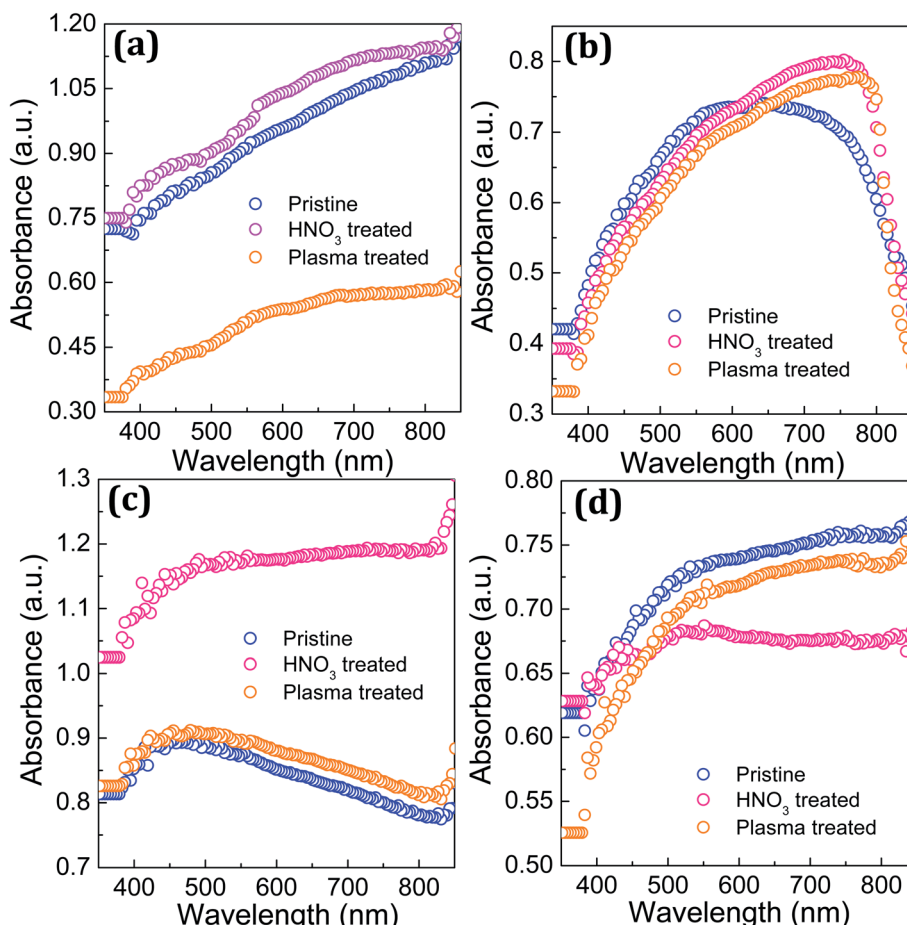


Fig. 7 Optical absorption of CdTe films grown on (a) Cu, (b) Al, (c) Ni and (d) SS foil showing the variation due to  $\text{HNO}_3$  and plasma treatment with respect to pristine substrates.

(~800 nm).<sup>35,46</sup> In contrast, Fig. 7(b) shows well saturated optical absorption obtained from CdTe grown on Al substrates with  $\text{HNO}_3$  and plasma treatment. Maximum optical absorption in the CdTe films was obtained at the band-edge position in the wavelength scale as shown. In the case of CdTe on the Al substrate, all three CdTe films (pristine,  $\text{HNO}_3$  and plasma treated) exhibited a similar trend in terms of reaching the maximum and falling in the longer wavelength region as shown in Fig. 7(b). The CdTe film on the Ni substrate showed features similar to CdTe on the Cu substrate but the magnitudes for  $\text{HNO}_3$  and plasma treatment were higher than the magnitude of absorption occurring in the pristine CdTe film. In this case also,  $\text{HNO}_3$  treatment yielded better absorbance compared with plasma treated CdTe. In contrast to Cu, Al, and Ni substrates, CdTe films grown on the SS substrate showed improved photo-absorption in the pristine state compared with CdTe grown on  $\text{HNO}_3$  and plasma treated SS substrates. In conclusion, it was observed that photo-interaction in CdTe is highly sensitive to the morphologies determined by the substrates used to grow CdTe films.<sup>35,46</sup> A further change in morphology due to  $\text{HNO}_3$  and plasma treatment also influenced the absorption significantly. The change in absorption was observed to be very unique depending on substrates and the surface treatments which

eventually determine the morphology of the resulting CdTe films. Further, optical bandgap values of the CdTe films were calculated using the Tauc plot method and the values are listed in Table 3.

Fig. 8 shows the *I*-*V* characteristics of the CdTe films grown on (a) Cu, (b) Al, (c) Ni and (d) SS foil showing the variation due to  $\text{HNO}_3$  and plasma treatment with respect to the pristine substrates measured under dark conditions. The measured current under dark conditions in the CdTe film grown on pristine Cu substrates was lower compared with the current values exhibited by CdTe on Cu substrates subjected to  $\text{HNO}_3$  and plasma treatment.

Table 3 Optical bandgap of CdTe films coated on Cu, Al, Ni and SS foil

Substrates	Optical bandgap (eV)		
	Pristine	$\text{HNO}_3$ treated	Plasma treated
Cu	1.28	1.34	1.39
Al	1.43	1.46	1.48
Ni	1.39	1.35	1.37
SS	1.33	1.45	1.30

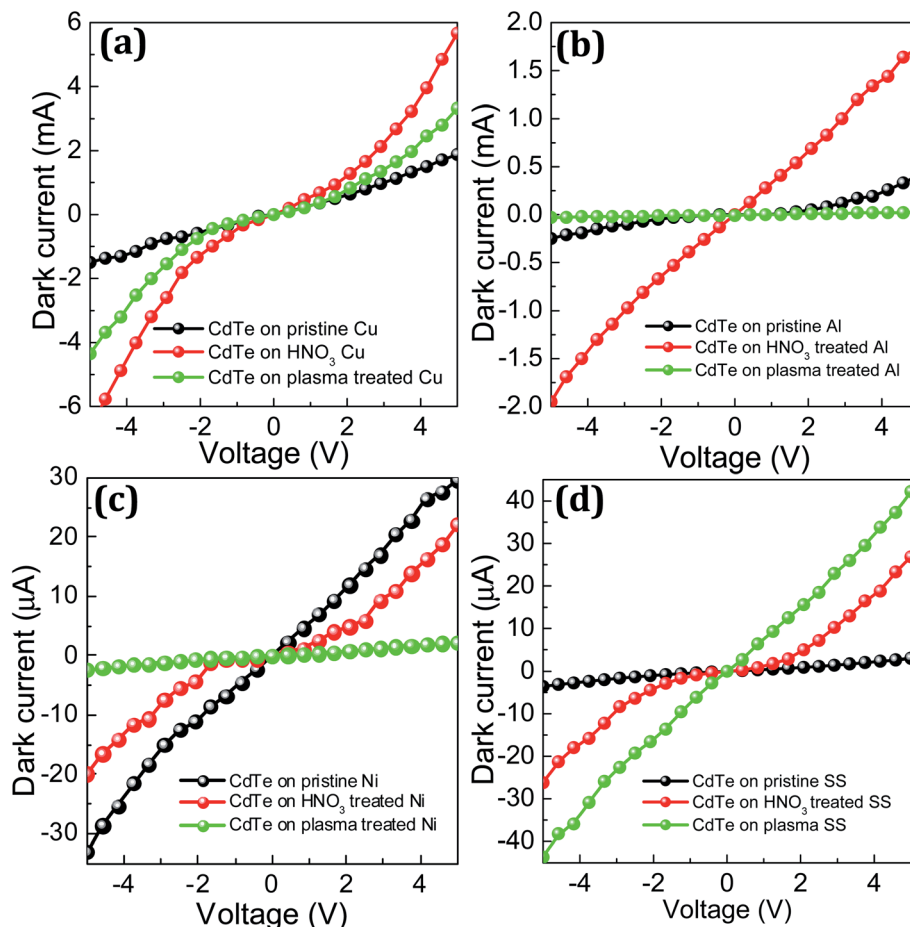


Fig. 8 Dark  $I$ – $V$  characteristics of the CdTe films grown on (a) Cu, (b) Al, (c) Ni and (d) SS foil showing the variation due to  $\text{HNO}_3$  and plasma treatment with respect to pristine substrates.

Further, CdTe on Cu with  $\text{HNO}_3$  treatment resulted in higher current values compared to CdTe on plasma treated Cu. It is evident from the dark  $I$ – $V$  values that  $\text{HNO}_3$  treatment on Cu substrates facilitated charge transport. In the case of CdTe grown on the Al substrate also,  $\text{HNO}_3$  treatment raised the dark current significantly while the plasma treatment suppressed the same to lower than that for CdTe on the pristine Al substrate as shown in Fig. 8(b). In contrast to CdTe on Cu and Al substrates, the dark current values measured from CdTe on the pristine Ni substrate were higher than the current values obtained from CdTe on the  $\text{HNO}_3$  and plasma treated Ni substrates as shown in Fig. 8(c). The dark current measured from CdTe on the pristine SS substrate was lower compared with that from CdTe on  $\text{HNO}_3$  and plasma treated SS substrates as shown in Fig. 8(d). From all these observations, it is inferred that charge transport in CdTe is highly morphology dependent and can further be engineered by surface treatment techniques. Table 4 lists the dark current values obtained from CdTe films coated on Cu, Al, Ni and SS substrates at a 5 V applied bias. In the case of CdTe on Cu and Al, the  $\text{HNO}_3$  treatment resulted in higher dark current values of 5.67  $\mu\text{A}$  and 1.74  $\mu\text{A}$ , respectively. CdTe on the pristine Ni substrate resulted in a dark current of 29.7  $\mu\text{A}$  and CdTe on the SS substrate showed a maximum dark current of 42.2  $\mu\text{A}$

under the influence of plasma treatment. This shows that each metallic substrate is entirely different in coating CdTe films whose electrical transport characteristics are highly influenced by substrates and further surface treatments.

Fig. 9 shows the illuminated  $I$ – $V$  characteristics of the CdTe films grown on (a) Cu, (b) Al, (c) Ni and (d) SS foil showing the variation due to  $\text{HNO}_3$  and plasma treatment with respect to pristine substrates. Similar to the dark  $I$ – $V$  characteristics, the morphology changes in CdTe films influenced the illuminated  $I$ – $V$  characteristics. In the case of CdTe on the Cu substrate, the pristine Cu enabled CdTe to exhibit lower illuminated current compared to CdTe on  $\text{HNO}_3$  and plasma treated Cu substrates.

Table 4 Variation of dark current values with respect to substrates and surface treatments

Substrates	Dark current ( $\mu\text{A}$ ) @ 5 V		
	Pristine	$\text{HNO}_3$ treated	Plasma treated
Cu	1.88	5.67	3.32
Al	0.41	1.74	0.03
Ni	29.7	22.1	2.13
SS	3.01	26.9	42.2



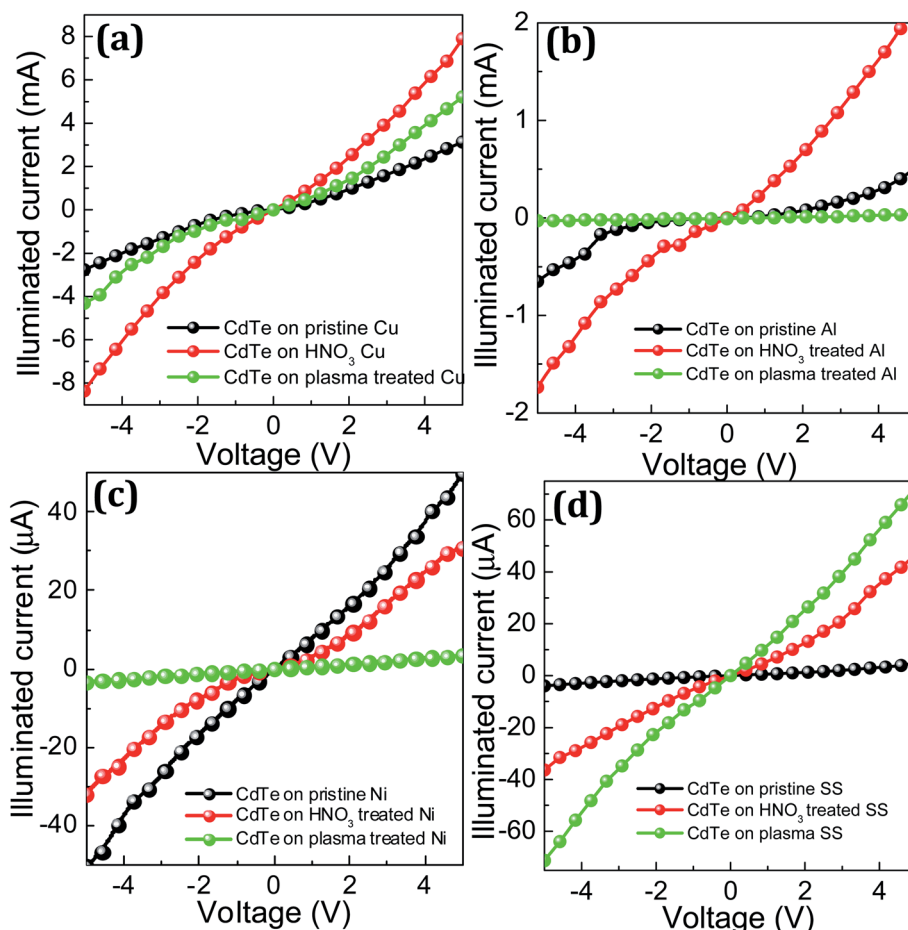


Fig. 9 Illuminated  $I$ – $V$  characteristics of the CdTe films grown on (a) Cu, (b) Al, (c) Ni and (d) SS foil showing the variation due to  $\text{HNO}_3$  and plasma treatment with respect to pristine substrates.

As demonstrated in the dark  $I$ – $V$  characteristics of Al substrates in Fig. 8(b), the illuminated  $I$ – $V$  characteristics obtained from CdTe on Al substrates showed the same trend. Fig. 9(c) and (d) confirm that similar features were obtained in illuminated current measured from CdTe on Ni and SS substrates as observed in the case of dark conditions. In general, excess carriers are generated under illumination which as a result exhibited improved current compared to the corresponding dark current values. However, it is essential to consider the electronic quality of the charge transport pathway in CdTe and the morphology at the nanoscale as influential parameters which interact with electrons and holes. While surface treatment increased the current values in CdTe films on the reported four substrates, it is easy to understand that the charge transport pathways are less influenced by defects. The wet-chemical and gas-phase surface treatments energetically modified the morphology which in turn resulted in a change in current. However, it is not simply the same in all four metallic substrates as the morphology undergoes rigorous changes. Thus, it is also essential to consider the morphological effect on charge transport. Table 5 lists all the illuminated current values measured from CdTe films coated on Cu, Ni, Al, and SS substrates measured at a 5 V applied bias. As observed in the dark current

values, CdTe on Cu and Al substrates showed higher illuminated current values of 7.9  $\mu\text{A}$  and 2.2  $\mu\text{A}$ , respectively. This similarity between dark and illuminated current values from CdTe on Cu and Al can be attributed to the  $\text{HNO}_3$  surface treatment on Cu and Al substrates which form good quality CdTe films in which effective charge transport occurred compared to pristine and plasma treated ones. CdTe films on Ni and SS substrates showed higher illuminated current values of 49.8  $\mu\text{A}$  and 73  $\mu\text{A}$  under pristine and plasma treatment. This situation is also very similar to the dark current measured from the CdTe on Ni and SS substrates. Thus, the current values

Table 5 Variation of illuminated current values with respect to substrates and surface treatments

Substrates	Illuminated current ( $\mu\text{A}$ ) @ 5 V		
	Pristine	$\text{HNO}_3$ treated	Plasma treated
Cu	3.13	7.90	5.22
Al	0.52	2.21	0.04
Ni	49.8	31.0	3.14
SS	5.08	47.0	73.0

measured under illumination confirm that they are all in good agreement with dark current values.

The morphological features in functional materials play optically and electronically active roles as they determine light-matter interactions. For example, photon management in textured semiconductor surfaces is entirely different from that in the same semiconductors with a planar surface. Similarly, charge transport in terms of electrons and holes also differs with morphological order. The morphological features in semiconductors directly participate in charge carrier scattering and collision and determine the overall diffusion length which eventually results in the magnitude of the current values measured. The present work accounted for both the change in the morphological order influenced by surface treatment on substrates and, as a result of this, the change in charge transport characteristics. Various possible micro/nanostructures acquired in CdTe due to various approaches/substrates and their influence on physical properties are listed in the ESI section.†

## Conclusions

The microstructural characteristics of CdTe films were highly dependent upon the morphology of the metallic foil used as the substrate. Wet-chemical ( $\text{HNO}_3$ ) and Ar-plasma modified metal surfaces effectively engineered CdTe growth and resulted in (i) vertically aligned walls, (ii) valley–hills and (iii) micro-granules. Further, studies asserted that the charge transport characteristics in CdTe films were highly influenced by the morphological features as observed from the changes in  $I$ – $V$  characteristics both under dark and illuminated conditions.

## Conflicts of interest

There are no conflicts to declare.

## Acknowledgements

The authors thank the Amrita Centre for Nanosciences for providing the PVD Cluster facility through industry support to perform CdTe coating and plasma processing on functional materials for energy conversion applications.

## References

- 1 J. Misiewicz, G. Sek, R. Kudrawiec and P. Sitarek, *Thin Solid Films*, 2004, **450**, 14–22.
- 2 B. Pasenow, M. Reichelt, T. Stroucken, T. Meier, S. W. Koch, A. R. Zakharian and J. V. Moloney, *J. Opt. Soc. Am. B*, 2005, **22**, 2039–2048.
- 3 K. S. Novoselov, D. Jiang, F. Schedin, T. J. Booth, V. V. Khotkevich, S. V. Morozov and A. K. Geim, *Proc. Natl. Acad. Sci. U. S. A.*, 2005, **102**, 10451–10453.
- 4 C. Weisbuch, H. Benisty and R. Houdré, *J. Lumin.*, 2000, **85**, 271–293.
- 5 P. Vasa and C. Lienau, *ACS Photonics*, 2018, **5**, 2–23.
- 6 L. Sortino, P. G. Zotev, S. Mignuzzi, J. Cambiasso, D. Schmidt, A. Genco, M. Aßmann, *et al.*, *Nat. Commun.*, 2019, **10**, 1–8.
- 7 L. Britnell, R. M. Ribeiro, A. Eckmann, R. Jalil, B. D. Belle, A. Mishchenko, Y.-J. Kim, *et al.*, *Science*, 2013, **340**, 1311–1314.
- 8 B. Piccione, C. O. Asperti, C.-H. Cho and R. Agarwal, *Rep. Prog. Phys.*, 2014, **77**, 086401.
- 9 L. Baraban and V. Z. Lozovski, *Opt. Spectrosc.*, 2004, **97**, 810–816.
- 10 V. Garg, B. Kamaliya, R. G. Mote and J. Fu, *MRS Commun.*, 2020, **10**, 135–140.
- 11 A. Deinega, I. Valuev, B. Potapkin and Y. Lozovik, *Opt. Lett.*, 2010, **35**, 106–108.
- 12 G. Köppel, B. Rech and C. Becker, *Nanoscale*, 2016, **8**, 8722–8728.
- 13 S. J. Cho, T. An and G. Lim, *Chem. Commun.*, 2014, **50**, 15710–15713.
- 14 L. Yao and J. He, *Prog. Mater. Sci.*, 2014, **61**, 94–143.
- 15 P. Spinelli, M. A. Verschueren and A. Polman, *Nat. Commun.*, 2012, **3**, 1–5.
- 16 M. N. Huda and J. A. Turner, *J. Appl. Phys.*, 2010, **107**, 123703.
- 17 S.-L. Wu, G.-A. Cheng, R.-T. Zheng and X.-L. Wu, *J. Korean Phys. Soc.*, 2013, **63**, 1189–1193.
- 18 E. Menard, A. Marchenko, V. Podzorov, M. E. Gershenson, D. Fichou and J. A. Rogers, *Adv. Mater.*, 2006, **18**, 1552–1556.
- 19 F. Nasirpouri, I. Yousefi, E. Moslehifard and J. Khalil-Allafi, *Surf. Coat. Technol.*, 2017, **315**, 163–171.
- 20 A. Vasanth, S. V. Nair and M. Shanmugam, *Appl. Surf. Sci.*, 2020, **519**, 146263.
- 21 L. Zhang, J. Yang, X. Zhao, X. Xiao, F. Sun, X. Zuo and J. Nan, *Chem. Eng. J.*, 2020, **380**, 122546.
- 22 D. Meggiolaro, E. Mosconi, A. H. Proppe, R. Quintero-Bermudez, S. O. Kelley, E. H. Sargent and F. De Angelis, *ACS Energy Lett.*, 2019, **4**, 2181–2184.
- 23 T. P. Weiss, B. Bissig, T. Feurer, R. Carron, S. Buecheler and A. N. Tiwari, *Sci. Rep.*, 2019, **9**, 1–13.
- 24 S. Yang, C. Zhang, Z. Yang, J. Yao, H. Wang and G. Ding, *J. Alloys Compd.*, 2019, **778**, 90–96.
- 25 T. Gu, E.-T. Hu, S. Guo, Y. Wu, J. Wang, Z.-Y. Wang, K.-H. Yu, *et al.*, *Vacuum*, 2019, **163**, 69–74.
- 26 S. T. Kim, L. Larina, J. H. Yun, B. Shin and B. T. Ahn, *Sustainable Energy Fuels*, 2019, **3**, 709–716.
- 27 Q. Jiang, Y. Zhao, X. Zhang, X. Yang, Y. Chen, Z. Chu, Q. Ye, X. Li, Z. Yin and J. You, *Nat. Photonics*, 2019, **13**, 460–466.
- 28 W. K. Metzger, S. Grover, D. Lu, E. Colegrave, J. Moseley, C. L. Perkins, X. Li, *et al.*, *Nat. Energy*, 2019, **4**, 837–845.
- 29 E. Camacho-Espinosa, A. López-Sánchez, I. Rimmaudo, R. Mis-Fernández and J. L. Peña, *Sol. Energy*, 2019, **193**, 31–36.
- 30 K. Shen, Z. Bai, Y. Deng, R. Yang, D. Wang, Q. Li and D. Wang, *RSC Adv.*, 2016, **6**, 52326–52333.
- 31 R. Sekine, M. Uenomachi, H. Asafusa, K. Tokiwa, K. Shimazoe, H. Takahashi, Y. Harada, A. Fujimoto, T. Hirai and S. Sakuragi, *Cryst. Growth Des.*, 2019, **19**, 6218–6223.



32 Y. Wang, X. Huang, D. Wu, R. Zhuo, E. Wu, C. Jia, Z. Shi, T. Xu, Y. Tian and X. Li, *J. Mater. Chem. C*, 2018, **6**(18), 4861–4865.

33 M. Shaygan, K. Davami, N. Kheirabi, C. K. Baek, G. Cuniberti, M. Meyyappan and J.-S. Lee, *Phys. Chem. Chem. Phys.*, 2014, **16**, 22687–22693.

34 X. Xie, S.-Y. Kwok, Z. Lu, Y. Liu, Y. Cao, L. Luo, J. A. Zapien, *et al.*, *Nanoscale*, 2012, **4**, 2914–2919.

35 L. K. Jambi, J. E. Lees, S. L. Bugby, S. Tipper, M. S. Alqahtani and A. C. Perkins, *J. Instrum.*, 2015, **10**, P06012.

36 M. Powalla, S. Paetel, E. Ahlsweide, R. Wuerz, C. D. Wessendorf and T. Magorian Friedlmeier, *Appl. Phys. Rev.*, 2018, **5**, 041602.

37 C. K. Miskin, A. Dubois-Camacho, M. O. Reese and R. Agrawal, *J. Mater. Chem. C*, 2016, **4**, 9167–9171.

38 S. Kumar and K. S. R. Koteswara Rao, *Energy Environ. Sci.*, 2014, **7**, 45–102.

39 J. C. Quiñones-Galván, A. Guillén-Cervantes, E. Campos-González, J. Santos-Cruz, S. A. Mayén-Hernández, M. de la L. Olvera, O. Zelaya-Angel, G. Contreras-Puente and F. de Moure-Flores, *J. Laser Appl.*, 2016, **28**, 032012.

40 A. M. Ali, K. S. Rahman, L. M. Ali, M. Akhtaruzzaman, K. Sopian, S. Radiman and N. Amin, *Results Phys.*, 2017, **7**, 1066–1072.

41 B. E. McCandless and J. R. Sites, *Handbook of Photovoltaic Science and Engineering*, 2011, pp. 600–641.

42 A. Bosio, N. Romeo, S. Mazzamuto and V. Canevari, *Prog. Cryst. Growth Charact. Mater.*, 2006, **52**, 247–279.

43 A. Morales-Acevedo, *Sol. Energy*, 2006, **80**, 675–681.

44 J. L. Plaza, O. Martínez, S. Rubio, V. Hortelano and E. Diéguez, *CrystEngComm*, 2013, **15**, 2314–2318.

45 J. M. Lugo, E. Rosendo, R. Romano-Trujillo, A. I. Oliva, H. Pérez Ladrón de Guevara, C. I. Medel-Ruiz, L. Treviño-Yarce, *et al.*, *Mater. Res. Express*, 2019, **6**, 076428.

46 S. L. Patel, S. Chander, M. D. Kannan and M. S. Dhaka, *Appl. Surf. Sci.*, 2019, **498**, 143824.

47 D. Zhou, M. Lin, Z. Chen, H. Sun, H. Zhang, H. Sun and B. Yang, *Chem. Mater.*, 2011, **23**, 4857–4862.

48 J.-H. Yang, W.-J. Yin, J.-S. Park, J. Ma and S.-H. Wei, *Semicond. Sci. Technol.*, 2016, **31**, 083002.

49 D. Krasikov and I. Sankin, *J. Mater. Chem. A*, 2017, **5**, 3503–3513.

50 J. M. Burst, S. B. Farrell, D. S. Albin, E. Colegrave, M. O. Reese, J. N. Duenow, D. Kuciauskas and W. K. Metzger, *APL Mater.*, 2016, **4**, 116102.

51 I. M. Dharmadasa, *Coatings*, 2014, **4**, 282–307.

52 V. Komin, B. Tetali, V. Viswanathan, S. Yu, D. L. Morel and C. S. Ferekides, *Thin Solid Films*, 2003, **431**, 143–147.

53 S. Yao, L. Liu, Q. Zeng, X. Du, C. Im, Y. Liu, H. Zhang, B. Yang, T. Cui and W. Tian, *J. Mater. Chem. C*, 2018, **6**(41), 11156–11161.

54 M. O. Reese, J. M. Burst, C. L. Perkins, A. Kanevce, S. W. Johnston, D. Kuciauskas, T. M. Barnes and W. K. Metzger, *IEEE J. Photovolt.*, 2014, **5**, 382–385.

55 G. I. García-Alvarado, F. de Moure-Flores, S. A. Mayén-Hernández, D. Santos-Cruz, E. M. Rivera-Muñoz, G. S. Contreras-Puente, M. Pal and J. Santos-Cruz, *Vacuum*, 2017, **142**, 175–180.

56 M. Arreguín-Campos, K. Gutiérrez ZB, J. G. Quiñones-Galván, J. Santos-Cruz, S. A. Mayén-Hernández, O. Zelaya-Angel, M. de la L. Olvera, G. Contreras-Puente and F. de Moure-Flores, *J. Electron. Mater.*, 2019, **48**, 3595–3602.

